Stable Interphase Chemistry of Textured Zn Anode for Rechargeable Aqueous Batteries

Jindi Wang[1,†], Bao Zhang[2,†], Zhao Cai[1,†], Renming Zhan[1], Wenyu Wang[1], Lin Fu[1], Mintao Wan[1], Run Xiao[1], Yangtao Ou[1], Li Wang[3], Jianjun Jiang[2], Zhi Wei Seh[4], Hong Li[5], and Yongming Sun[1,*]

1 Wuhan National Laboratory for Optoelectronics, Huazhong University of Science and Technology, Wuhan, 430074, China
2 School of Optical and Electronic Information, Huazhong University of Science and Technology, Wuhan, 430074, China
3 Institute of Nuclear & New Energy Technology, Tsinghua University, Beijing, 100084, China
4 Institute of Materials Research and Engineering, Agency for Science, Technology and Research (A*STAR), 2 Fusionopolis Way, Innovis, 138634, Singapore
5 Institute of Physics, Chinese Academy of Sciences, Beijing 100190, China
† These authors contributed equally to this work.
* Correspondence author. Email: yongmingsun@hust.edu.cn.

Abstract
Despite the advances of aqueous zinc (Zn) batteries as sustainable energy storage systems, their practical application remains challenging due to the issues of spontaneous corrosion and dendritic deposits at the Zn metal anode. In this work, conformal growth of zinc hydroxide sulfate (ZHS) with dominating (001) facet was realized on (002) plane-dominated Zn metal foil fabricated through a facile thermal annealing process. The ZHS possessed high Zn^{2+} conductivity (16.9 mS cm^{-1}) and low electronic conductivity (1.28×10^4 Ω cm), and acted as a heterogeneous and robust solid electrolyte interface (SEI) layer on metallic Zn electrode, which regulated the electrochemical Zn plating behavior and suppressed side reactions simultaneously. Moreover, low self-diffusion barrier along the (002) plane promoted the 2D diffusion and horizontal electrochemical plating of metallic Zn for (002)-textured Zn electrode. Consequently, the as-achieved Zn electrode exhibited remarkable cycling stability over 7000 cycles at 2 mA cm^{-2} and 0.5 mAh cm^{-2} with a low overpotential of 25 mV in symmetric cells. Pairing with a MnO_2 cathode, the as-achieved Zn electrode achieved stable cell cycling with 92.7 % capacity retention after 1000 cycles at 10 *C* with a remarkable average Coulombic efficiency of 99.9 %.

Keywords: Rechargeable aqueous batteries, Zn metal anode, Interfacial chemistry, Zinc hydroxide sulfate, Electrochemical performance

1 Introduction

Worldwide concerns about global warming and energy crisis increase the urgency to develop sustainable energy (e.g., solar, wind, and tidal) technologies that include energy conversion, storage and utilization with low cost and high safety [1-5]. Rechargeable batteries with Zn metal anode and mild aqueous electrolyte have attracted extensive attention for large-scale energy storage due to both intrinsic safety and cost-effectiveness [6-15]. For instance, the material cost for aqueous Zn metal batteries is estimated to be US$21.43/kWh, which is less than a third of that for current lithium ion batteries (US$70.96/kWh, Table S1 online). However, Zn metal anode is

thermodynamically unstable in aqueous electrolyte, as exemplified by the spontaneous corrosion and electrochemical dendritic deposition of metallic Zn [16-20]. Various strategies, including introducing polymer corrosion inhibition layer [21] and employing additive ions in the electrolyte [22], have been proposed to achieve highly reversible aqueous Zn metal electrodes. Notably, building an artificial solid-electrolyte-interface (SEI) with poor electronic conductivity and high ionic conductivity can avoid the direct chemical or electrochemical reactions between active Zn metal and electrolyte, and ensure fast Zn^{2+} transfer simultaneously [19, 23-26]. However, it remains challenging to fabricate homogeneous and stable artificial SEI for long-term cycling. Inhomogeneous artificial SEI could be cracked and even detached from Zn metal electrodes during cycling. Also, ionic conductivity of many reported artificial SEIs on Zn metal electrode is often unsatisfactory (e.g. < 1 mS cm^{-1}), especially for a battery running under fast-charging/discharging conditions. Therefore, construction of robust SEI with high ionic conductivity is of significant importance yet challenging for realizing high-performance aqueous Zn metal electrodes.

Electrochemical reactions between electrolyte (usually the additive) and active metal have been widely utilized to *in-situ* construct a surface protection layer (artificial SEI layer) during electrochemical cycling for various battery anodes (e.g., vinylene carbonate for Si anode in lithium-ion batteries, $LiNO_3$ for lithium anode in lithium metal batteries, and fluoroethylene carbonate for hard carbon anode in sodium-ion batteries) [27-29]. In the case of aqueous Zn chemistry, Zn metal chemically reacts with aqueous electrolyte spontaneously after the battery assembly before its cycling, producing $Zn(OH)_2$/zinc hydroxide sulfate (ZHS), accompanied by the consumption of electrolyte and active Zn metal [30, 31]. The as-formed ZHS byproducts are generally micrometer-size sheets and stacked randomly to form a loose surface layer on metallic Zn. Corrosion would take place continuously on Zn metal electrode to produce ZHS [19, 32], and thus ZHS has long been treated/understood as harmful side products. Thus far, the most common method to tackle the corrosion issue is to construct artificial SEI by electrochemical decomposition of electrolyte additives [33-35]. However, spontaneous chemical corrosion reactions can occur before the electrochemical formation of artificial SEI, which would make the electrolyte additives insufficient to protect Zn metal anode in regular aqueous electrolytes. We propose to utilize the spontaneous reactions between metallic Zn and electrolyte, and regulate the production of ZHS for Zn metal protection. In principle, if a dense and uniform ZHS layer could form on metallic Zn surface, the direct contact between Zn metal and liquid electrolyte would be cut off, and the chemical corrosion of metallic Zn would be significantly hindered. Besides the conformal formation of a robust protection layer, high Zn^{2+} ion conductivity and low electronic conductivity of such specific layer are also of key importance for realizing stable electrochemical Zn plating/stripping [33]. However, few reports have paid attention to the chemical and physical properties of such "harmful" ZHS in battery studies. Thus, it is of vital importance to reveal the hidden chemistry/physics of ZHS and its controlled growth, which could provide new insights for improving Zn metal anode.

In this study, epitaxial growth of homogeneous and dense (001) plane-dominated ZHS layer was realized on (002)-textured Zn metal foil electrode [denoted as (002)-Zn electrode] that was fabricated by a simple thermal annealing process, enabling highly-reversible aqueous Zn metal batteries. A homogeneous ZHS layer with dominating (001) facet was built on the surface of (002)-Zn electrode after resting in $ZnSO_4$ electrolyte, which exhibited high Zn^{2+}-ion conductivity (16.9 mS cm^{-1}) and low electronic conductivity (1.28×10^4 Ω cm). The (002)-Zn electrode showed significantly

suppressed corrosion and produced 9 times lower hydrogen volume in comparison to a pristine Zn electrode. Also, the (002) plane of as-achieved electrode allowed low self-diffusion barrier, leading to horizontal electrodeposition of metallic Zn. Symmetrical cells assembled by (002)-Zn metal electrodes showed stable Zn stripping/plating for 7000 cycles with a low overpotential of 25 mV at 2 mA cm^{-2} and 0.5 mAh cm^{-2}. MnO_2||(002)-Zn full cells exhibited a moderately high capacity of 83.6 mAh g^{-1} under 10 *C* and excellent cycling stability for 1000 cycles with 92.7% capacity retention, far outperforming the MnO_2||Zn counterparts measured under the same condition (showing only 34.9 % capacity retention after 100 cycles).

2 Materials and methods

2.1 Preparation of (002)-Zn foil electrode

The (002)-Zn foils were prepared by annealing commercial Zn metal foils under a flowing 5% Ar/H_2 gas at 300 ºC for 60 min. Subsequently, the Zn foils were cooled down naturally to room temperature and stored in a glove box before further use.

2.2 Materials characterization

X-ray diffraction (XRD) patterns were conducted on a PANalytical B.V., Holland with Cu Kα radiation (λ = 0.145 nm). The texture coefficients (T_c) of Zn metal were calculated according to the following formula:

$$T_{c(hkl)} = \frac{I_{(hkl)}/I_{0(hkl)}}{\sum(I_{(hkl)}/I_{0(hkl)})} \times 100\%$$

Where $T_{c(hkl)}$ was the texture coefficient of the (hkl) facet, $I_{(hkl)}$ was the diffraction intensities of the (hkl) facet measured in the XRD for the Zn sample, and $I_{o(hkl)}$ was the diffraction intensities of the (hkl) facet for the standard Zn sample (PDF#04-0831). Scanning electron microscopy (SEM) and energy dispersive X-ray spectroscopy (EDX) elemental mapping images and EDX spectrums were collected by using a field-emission SEM instrument (GeminiSEM300). The electron backscattered diffraction (EBSD) measurements were performed on an orientation imaging microscopy (OIM) data collection on a SEM (GeminiSEM300). The pristine Zn and (002)-Zn foils were ion milled using a precision-ion-polishing system (Gatan PSPS Ⅱ 695) before EBSD measurements. Optical microscopy (OM) images were collected on an Olympus BX53 light microscope equipped with LED lamp and CMOS detector (DP27, Olympus). *In-situ* OM studies were carried out in 0.2 mol L^{-1} $ZnSO_4$ aqueous electrolyte using a home-made transparent cell. High resolution transmission electron microscopy (HRTEM) image and selected area electron diffraction (SAED) pattern of ZHS sheets were collected on a field emission transmission electron microscope (Tecnai G^2 F30, FEI).

2.3 Electrochemical measurements

Symmetrical cells were assembled with two pristine Zn foils or (002)-Zn foil electrodes in CR2032 type coin cells. Glass fiber (GF/A) and 3 mol L^{-1} $ZnSO_4$ aqueous solution were used as the separator and electrolyte, respectively. All cells were rested for 12 h before testing on Land battery tester. Electrochemical cycling behaviors were measured by galvanostatic charge and discharge at current density of 2–5 mA cm^{-2} with areal capacity of 0.5–5 mAh cm^{-2}. The electronic resistance and ionic conductivity were measured using a Biologic VMP3 electrochemical workstation with two blocking electrodes. The ZHS film for electrochemical measurements was prepared by pressing ZHS powder sample using an automatic tablet press. The ZHS powder was prepared

by a liquid-phase synthesis. Typically, 200 mL 0.2 mol L^{-1} $ZnSO_4$ aqueous solution was mixed with 200 mL 0.2 mol L^{-1} hexamethylenetetramine aqueous solution and 400 mL ethanol. After adjusting the pH to 5~6 using 0.5 mol L^{-1} H_2SO_4, the mixed solution was rested at 70 ºC for 2 h and then cooled to room temperature. Electrochemical impedance spectroscopy (EIS) data was collected at open-circuit voltage from 10^{-1} to 10^5 Hz with an AC voltage of 5 mV. The ionic conductivity was calculated by $\sigma = l/(R_b*S)$, where l was the thickness of the ZHS membrane, R_b was the resistance according to EIS, and S was the contact area between ZHS and blocking electrode. During the ionic conductivity measurement, a drop of aqueous $ZnSO_4$ electrolyte was employed for ZHS and glass fiber membranes to reflect the apparent ionic conductivity under the battery working conditions. Zn||Zn symmetric cell in a pouch configuration with an electrode size of 4×5 cm^2 was fabricated and the volume of hydrogen gas was extracted and recorded by a disposable syringe after resting. Full cells were assembled with the pristine Zn foils or (002)-Zn foils as the anodes, the MnO_2 as the cathode, the GF as the separator, and the 3 mol L^{-1} $ZnSO_4$ + 0.1 mol L^{-1} $MnSO_4$ solution as the electrolyte. The MnO_2 cathode were prepared by electrodeposition under 1.8 V for 8 h with a two-electrode system, where a carbon cloth was employed as working electrode, Zn foil was employed as the counter electrode, and 3 mol L^{-1} $ZnSO_4$ + 0.3 mol L^{-1} $MnSO_4$ was employed as electrolyte. The active mass loading of the cathode was about 0.5 mg cm^{-2}. The cycling performance was conducted on Land battery tester in the voltage range of 1.0–1.8 V.

2.4 Theoretical calculations

The DFT calculations [36, 37] were performed by using Vienna Ab-initio Simulation Package (VASP) [38] with Projector Augmented Wave (PAW) method [39]. The exchange-correlation energy was described by the functional of Perderw, Burke, and Ernzerhof (PBE) form [40, 41] including van der Waals corrections (DFT-D3 method) [42]. The kinetic energy cutoff of electron wave functions was 520 eV. The geometry optimizations were performed by using the conjugated gradient method, and the convergence threshold was set to be 10^{-4} eV in energy and 0.02 eV $Å^{-1}$ in force. The Brillouin zone was sampled by using the Monkhorst−Pack scheme [43]. The interface energy was evaluated using the same method in a previous work [44]. Visualization of the electrolyte structures were made by using VESTA [45]. The MEAM calculations were performed by using LAMMPS [46], the force field of Zn was taken from previous publications [47].

3 Results and discussion

3.1 Theoretical prediction of horizontal ZHS on $(002)_{Zn}$ plane

Figure 1a illustrates the corrosion and cycling of commercial (pristine) Zn electrodes in aqueous electrolyte. Chemical corrosion of metallic Zn produces sheet-like ZHS, which stacks randomly to form a loose corrosion layer on metallic Zn foil. The pore structure of the ZHS layer allows the penetration of electrolyte and its direct contact with fresh metallic Zn, leading to continuous corrosion side-reactions and increased thickness of the ZHS layer. Such ZHS layer would increase the interface resistance, aggravate the non-uniform plating behavior of metallic Zn, and eventually lead to rapid battery failure. However, if the reaction between Zn metal and aqueous electrolyte could produce a homogeneous and horizontal ZHS film on metallic Zn surface with high ionic conductivity, such ZHS layer would serve as a SEI to stabilize Zn metal electrode and improve the electrochemical reversibility of aqueous Zn batteries (Fig. 1b). In aqueous electrolyte system (typically $ZnSO_4$ electrolyte), metallic Zn reacts with

H_2O molecules to produce $Zn(OH)_2$, which would be transformed to ZHS due to the more stabilized crystalline structure [48]. Both $Zn(OH)_2$ and ZHS fall inside the well-known class of layered double hydroxides (LDH), which are derivative phases of the mineral brucite with extra anions and/or water molecules between the brucite layers [49]. The crystal structures and symmetries of the brucite support the sheet-like growth of $Zn(OH)_2$ and ZHS with (001) dominated crystal facet. $(001)_{brucite}$ facet and $(002)_{Zn}$ facet both possess hexagonal Bravais lattice, and share very similar crystallographic symmetry. Therefore, the affinity of $(001)_{brucite}$ with $(002)_{Zn}$ should be stronger than other facets of metallic Zn, such as $(101)_{Zn}$. As shown in Fig. 1c and Fig. S1 online, the interface energy of $(002)_{Zn}$-$(001)_{ZHS}$ is lower than the interface energy between other planes of Zn and $(001)_{ZHS}$ such as $(101)_{Zn}$-$(001)_{ZHS}$, indicating the higher affinity between $(002)_{Zn}$ facet and $(001)_{ZHS}$ facet. In this way, the ZHS may prefer horizontal and dense growth with dominating (001) facet along the $(002)_{Zn}$ facet. Besides, the higher ordered and flat surface atomic structure of $(002)_{Zn}$ gives a lower surface atom self-diffusion barrier (Fig. 1d and Fig. S2 online), which is beneficial for promoting the 2D diffusion of metallic Zn and inhibiting its dendritic growth during electrochemical plating process. Together, due to unique symmetry and high ordered structure of $(002)_{Zn}$ facet and $(001)_{ZHS}$ facet, the Zn metal electrode with (002) facet stands a good chance of *in-situ* generating horizontal ZHS to suppress corrosion side reactions and meanwhile promote 2D diffusion of metallic Zn to inhibit dendritic growth, thus realizing high electrochemical reversibility.

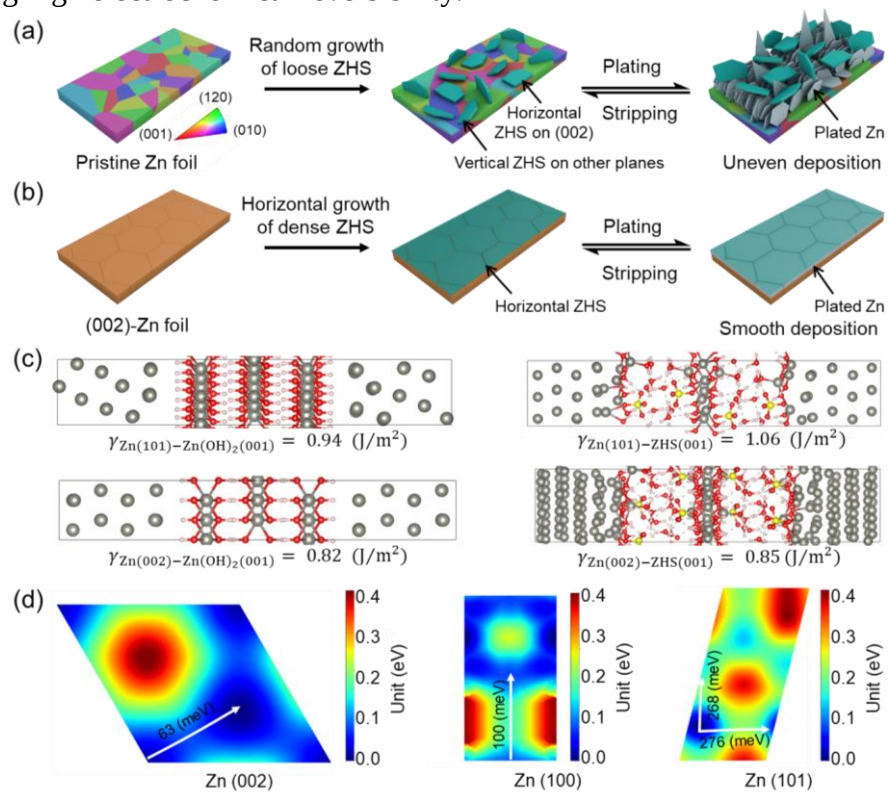

Fig. 1 Computational analysis of the SEI chemistry of aqueous Zn metal electrode. Schematic illustration of ZHS formation and electrochemical cycling of (a) pristine Zn electrode and (b) (002)-Zn electrode in $ZnSO_4$ aqueous electrolyte. Random growth of ZHS and its loose stacking lead to continuous corrosion of metallic Zn and degrade the electrochemical cycling of pristine Zn metal electrode. Dense ZHS layer forms on (002)-Zn electrode, which enables stable electrochemical cycling. (c) Interface energies of Zn-$Zn(OH)_2$ and Zn-ZHS, suggesting the thermodynamically favorable interface at Zn (002)-$Zn(OH)_2$ (001) and Zn (002)-ZHS (001). (d) Surface diffusion properties of

the three main crystal facets of Zn metal based on MEAM method, revealing the lowest diffusion energy of Zn atom on $(002)_{Zn}$ plane

3.2 Preparation and characterization of (002)-Zn electrode

In light of the above theoretical analyses, we sought to explore a controllable method to fabricate Zn metal electrode with dominating (002) facet. In the crystal structure of hexagonal metallic Zn, the (002) facet has the lowest surface energy among all its facets due to its close packed plane structure (Fig. 2a, 2b, and Fig. S3 online, Table S2 online). According to the classical metal annealing theory, annealing helps metal crystals transform into grains with the minimum surface energy [50]. Fig. 2c schematically illustrates the preparation process of (002)-Zn electrode. After annealing in Ar/H_2 atmosphere, the pristine Zn foil with random orientation transformed into (002)-Zn foil. Fig. 2d showed the XRD patterns of the (002)-Zn foil obtained after annealing at 300 ^oC for 60 min. The texture coefficient of the $(002)_{Zn}$ plane was up to 84 %, which was much higher than the pristine Zn foil (8 %), suggesting the (002)-dominating facets of Zn foil after annealing. SEM images showed that both the surface of pristine Zn and (002)-Zn foils were flat, and the (002)-Zn foil exhibited clear grain boundaries after annealing, suggesting the recrystallization during the annealing (Fig. 2e) [51]. EBSD was also employed to further analyze the texture information of (002)-Zn foil. As shown in Fig. 2f and 2h, the crystal plane of pristine Zn foil was random and disordered. In contrast, the (002)-Zn foil showed red series-dominated surface representing the (002) texture of metallic Zn. Polar graph was further conducted to investigate the texture of the (002)-Zn foil. The (001) polar figures demonstrated the texture change from the pristine Zn foil to (002)-Zn foil (Fig. 2g and 2i). The grains of pristine Zn foil were mainly vertical (normal of (001) facet parallel to Y0), while the grains of (002)-Zn foil were mainly horizontal (normal of (001) facet parallel to Z0). Moreover, the reverse pole figures also verified such transition (Fig. S6 online). All these XRD and EBSD results verified the (002)-dominated plane of Zn metal electrode after annealing.

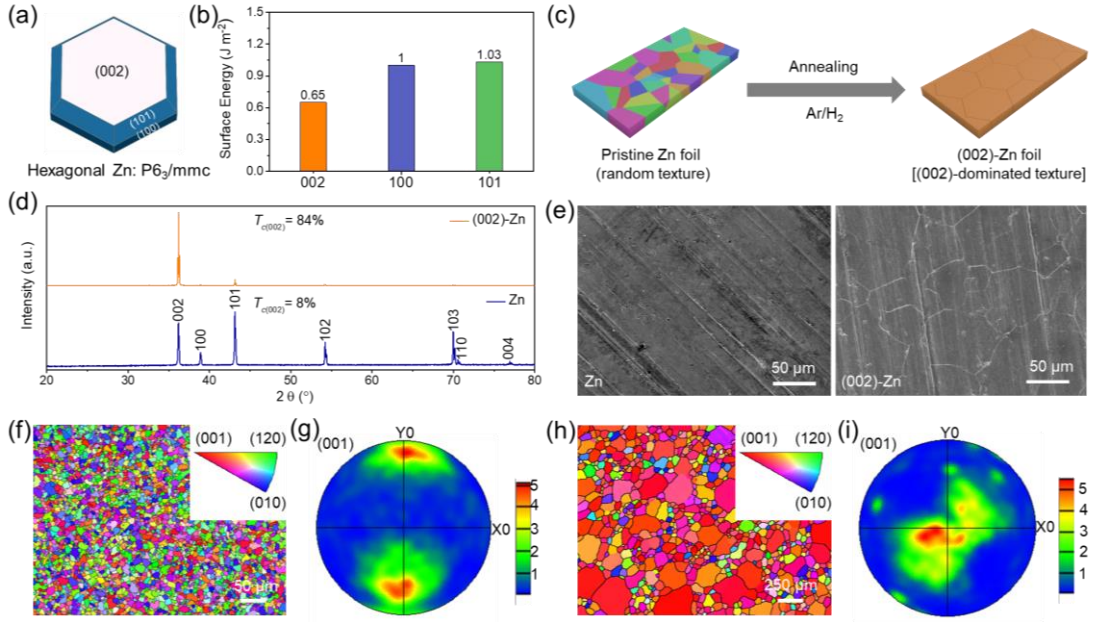

Fig. 2 Preparation and characterizations of (002)-Zn electrode. (a) Equilibrium crystal morphology of hexagonal metallic Zn by Wulff construction theory. (b) Surface energies of the main planes for hexagonal Zn metal. (c) Fabrication of (002)-Zn electrode via annealing in Ar/H_2 atmosphere. (d) XRD patterns of pristine Zn and (002)-Zn electrodes. (e) SEM images of pristine Zn and (002)-Zn electrodes. (f) EBSD

inverse pole figure (IPF) maps and (g) pole figures of pristine Zn electrode, (h) EBSD IPF maps and (i) pole figures of (002)-textured Zn electrode, revealing the (002) dominated crystal plane of the as-prepared (002)-Zn electrode

3.3 *In-situ* growth of horizontal ZHS

Pristine Zn and (002)-Zn electrodes were immersed in 3 mol L^{-1} $ZnSO_4$ aqueous electrolyte and rested for 7 days, and the morphology and structure of the as-formed ZHS on the surface of Zn metal electrodes were studied. The pristine Zn electrode became gray after resting in aqueous electrolyte. OM images showed that a large number of randomly distributed flakes with size of about 200 μm were produced on the surface of pristine Zn electrode (Fig. 3a). The SEM results also confirmed the formation of abundant flakes on pristine Zn electrodes (Fig. 3b), and the corresponding EDS elemental mapping results revealed the existence of Zn, O and S elements for these flakes, supporting the formation of flake-like ZHS (Fig. 3c). In contrast, the (002)-Zn electrode after resting in aqueous electrolyte displayed its initial metallic luster and no flakes were observed on the electrode surface under OM (Fig. 3d). Meanwhile, the (002)-Zn electrode remained a smooth surface (Fig. 3e) with the same elemental signals of Zn, O and S (Fig. 3f), supporting the formation of a horizontal layer of ZHS on the surface of the (002)-Zn electrode (Fig. 3f). HRTEM image of ZHS peeled from (002)-Zn electrode showed a thin sheet-like morphology with flat surface (Fig. 3g). Moreover, the SAED pattern in Fig. 3h indicated the clear diffraction spots of (100) and (010) facets, suggesting that the (001) facet was dominating, which agreed well with the theoretical findings in Fig. 1c. XRD measurement for both samples was further carried out. The XRD pattern of the pristine Zn electrode after resting in aqueous electrolyte showed strong XRD peaks of $Zn_4(OH)_6SO_4 \cdot 4H_2O$ and $Zn_4(OH)_6SO_4 \cdot 3H_2O$ besides metallic Zn (Fig. S7 online), revealing the severe corrosion of pristine Zn in aqueous electrolyte and the phase information of ZHS [19, 49]. In contrast, the (002)-Zn electrode after resting in aqueous electrolyte exhibited very weak XRD diffraction signal of ZHS. Note that the pristine Zn electrode corroded continuously in the aqueous electrolyte and produced a large number of H_2 bubbles (Fig. S8 online), while (002)-Zn electrode released few bubbles, suggesting its excellent anti-corrosion property in aqueous electrolyte. In order to quantitatively analyze the corrosion of pristine Zn and (002)-Zn electrodes, symmetric cells in a pouch cell configuration were assembled with the electrode size of 4 × 5 cm, and the hydrogen evolution rates for both cells were recorded. As shown in Fig. 3i, the pristine Zn electrode showed a high hydrogen evolution rate of 0.31 mL d^{-1}, and such a high hydrogen evolution rate remained over the entire measurement period of 7 days. As contrast, the (002)-Zn electrode displayed a low hydrogen evolution rate in the initial stage (0.12 mL d^{-1} for the 1st day), and there was almost no hydrogen gas produced in the following remaining time. The total amount of gas evolution within 7 days was 2.12 mL for the pristine Zn electrode, while that for the (002)-Zn electrode was only one-tenth (0.22 mL, Fig. S9 online), suggesting the significantly suppressed corrosion side-reactions at the (002)-Zn electrode.

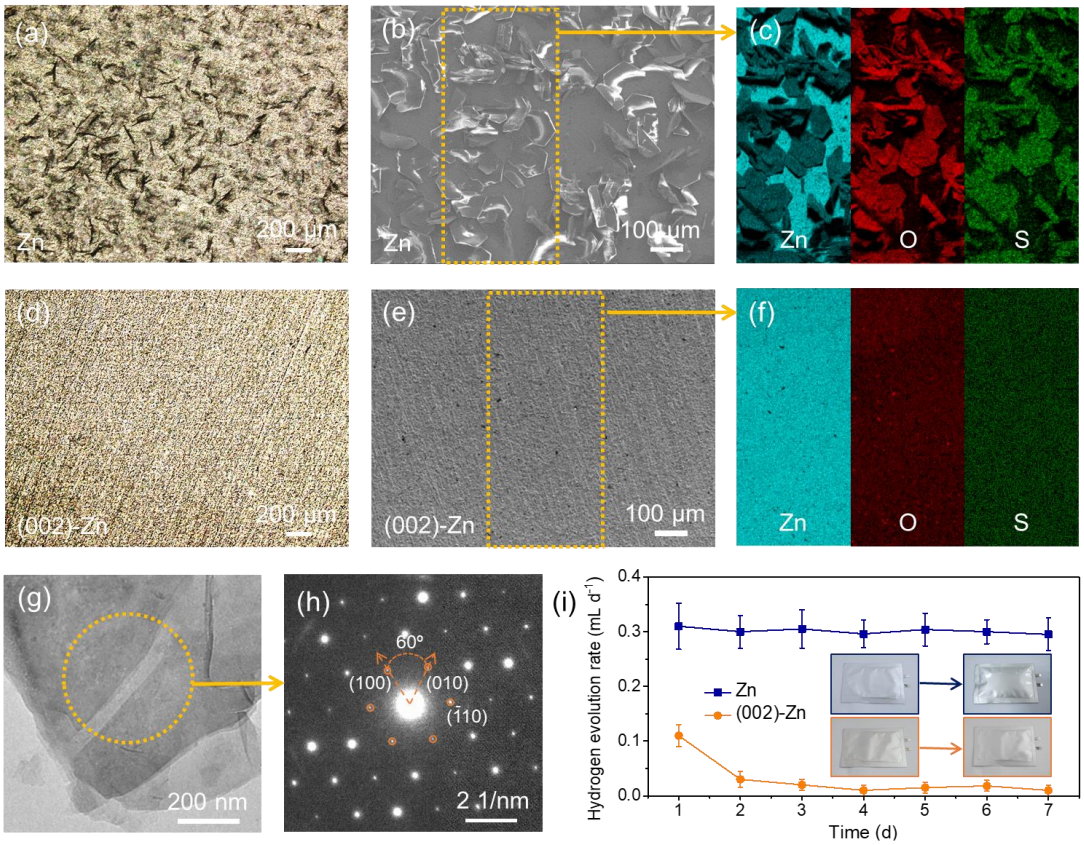

Fig. 3 Formation of horizontal ZHS on (002)-Zn electrode. (a) OM image, (b) SEM image, and (c) the corresponding EDS elemental mapping images of pristine Zn electrode after resting in aqueous $ZnSO_4$ electrolyte for 7 days. (d) OM image, (e) SEM image, and (f) EDS elemental mapping images of (002)-Zn electrode after resting in aqueous $ZnSO_4$ electrolyte for 7 days. (g) TEM and (h) SAED images of ZHS sheet peeled from a (002)-Zn electrode after resting in aqueous $ZnSO_4$ electrolyte for 7 days. These results indicate the horizontal growth of ZHS with dominating (001) facet. (i) The hydrogen evolution rates of pristine Zn and (002)-Zn electrodes in aqueous $ZnSO_4$ electrolyte. The inset shows digital images of a Zn||Zn and (002)-Zn||(002)-Zn symmetric cells before and after resting in aqueous $ZnSO_4$ electrolyte

3.4 Epitaxial electrodeposition of metallic Zn

An ideal SEI layer should possess both high ionic conductivity and low electronic conductivity. The ionic conductivity and electronic conductivity of the as-prepared ZHS film (Fig. S10 online) were evaluated. As shown in Fig. 4a and Fig. S11, Fig. S12 online, the ZHS membranes with different thicknesses showed a high apparent ionic conductivity of ~16.0 mS cm^{-1}, which was about 4 times that of a glass fiber (GF) separator with $ZnSO_4$ electrolyte (3.7 mS cm^{-1}). Meanwhile, the electronic resistivity of ZHS was determined to be 1.28×10^4 Ω cm, which was 3 orders of magnitude lower than that of Zn metal (13.3 Ω cm, Fig. 4a and Fig. S13 online). Therefore, the horizontal ZHS surface layer has the potential to serve as an ideal SEI to improve the electrochemical reversibility of metallic Zn anode. EIS was employed to investigate the ion transfer property of the horizontal ZHS surface layer. As shown in Fig. S14 online, the charge transfer resistance of the (002)-Zn electrode with horizontal ZHS before cycling was ~18 ohm, smaller than that of the pristine Zn electrode (~ 28 ohm). After 10 plating/stripping cycles, the charge transfer resistance of the pristine Zn electrode increased to ~130 ohm, which was caused by the formation of ZHS corrosion

products. Meanwhile, the charge transfer resistance of the (002)-Zn electrode with horizontal ZHS remained at ~18 ohm, demonstrating the important role of the horizontal ZHS surface layer in supressing corrosion side-reactions and promoting the ion transfer during cycling. In addition to the stable surface structure, (002) plane of the (002)-Zn electrode possesses the lowest theoretical self-diffusion barrier, thus improved 2D diffusion can be expected. As shown in Fig. 4b, the deposition current of the pristine Zn electrode under -150 mV reached a stable value after > 100 s, while the deposition current of the (002)-Zn electrode became stable within 30 s, suggesting a rapid 2D diffusion process for the (002)-Zn electrode [52], which was consistent with the DFT calculations. The morphology of the pristine Zn and (002)-Zn electrodes was further investigated by SEM after the electrodeposition of metallic Zn at 5 mA cm^{-2} and 5 mAh cm^{-2}. After electrodeposition (Fig. 4c and 4d), the Zn deposits were randomly distributed and nearly vertical to the electrode surface for a pristine Zn electrode, suggesting a slow diffusion process and high self-diffusion barrier, in accordance with the electrochemical analysis in Fig. 4b and the DFT results in Fig. 1d. Also, the nearly vertical metallic Zn deposits would easily pierce the separator, leading to short circuit of the batteries during electrochemical cycling. The (002)-Zn electrode after Zn plating showed a flat and compact surface morphology, which suggested the horizontal deposition of metallic Zn. The Zn deposition process was further monitored by *in-situ* OM. As shown in Fig. 4e and Movie S1 online, Zn dendrites were observed on the pristine Zn electrode after electrodeposition for 10 minutes at a current density of 10 mA cm^{-2}. With the increase of deposition time, the thickness of Zn deposition layer increased significantly, and it reached ~95 μm and evolved to a loose deposition layer after 30 minutes. In sharp contrast, the Zn deposition layer on (002)-Zn electrode remained dense and flat throughout the entire deposition process. The thickness of deposition layer was only 15 μm after 30 minutes of deposition (Fig. 4f and Movie S2 online), suggesting a much more uniform and dense electrochemical plating behavior. These direct *in-situ* results again demonstrated the uniform 2D electrodeposition of metallic Zn on (002)-Zn electrode, which made it highly promising for rechargeable aqueous batteries.

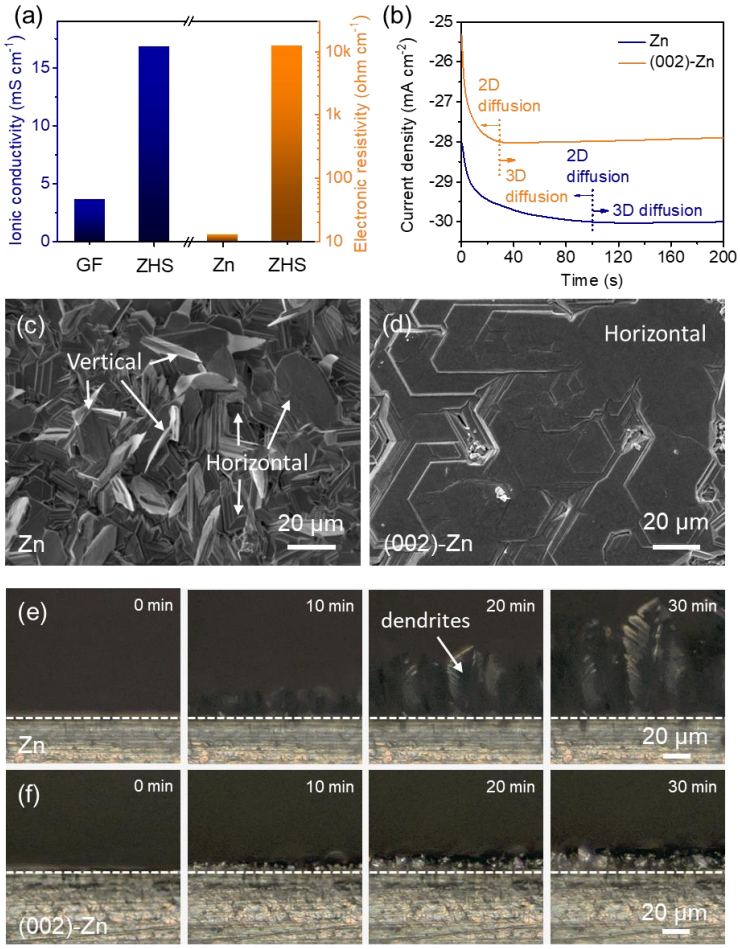

Fig. 4 The electrochemical plating behavior of (002)-Zn electrode. (a) The ionic conductivity of GF separator and ZHS, and the electronic resistivity of Zn metal and ZHS. (b) Chronoamperograms of pristine Zn and (002)-Zn electrodes at the overpotential of -150 mV. SEM images of (c) pristine Zn and (d) (002)-Zn electrodes after plating 5 mAh cm^{-2} of Zn at 5 mA cm^{-2}. *In-situ* OM images of the electrochemical plating behavior of (e) pristine Zn and (f) (002)-Zn electrodes at 10 mA cm^{-2}

3.5 Electrochemical performance of (002)-Zn electrode

To evaluate the electrochemical performance of (002)-Zn electrode in aqueous batteries, Zn||Zn and (002)-Zn||(002)-Zn symmetric cells were assembled and tested by galvanostatic cycling. Under a current density of 2 mA cm^{-2} with a fixed areal capacity of 0.5 mAh cm^{-2}, the (002)-Zn electrode exhibited stable plating/stripping cycling for 3500 h (Fig. 5a), which was among the best recently reported Zn metal electrodes (Table S3 online), demonstrating the superior electrochemical stability of the (002)-Zn electrode. Moreover, the (002)-Zn electrode showed stable and low overpotentials of 23 mV, 23 mV and 35 mV at the 10^{th}, 500^{th} and 7000^{th} cycle, respectively, showing superior electrochemical cycling stability. In sharp contrast, the pristine Zn electrode only lasted 200 h of cycling, and it encountered a sudden voltage hysteresis increase (300 mV after 268 h) and cell failure. Under a higher current density of 5 mA cm^{-2} and a fixed higher areal capacity of 2 mAh cm^{-2}, the (002)-Zn electrode still exhibited stable cycling for 250 h, while the pristine Zn electrode survived for only 30 h (Fig. 5b). Furthermore, the cycle life of (002)-Zn electrode reached 100 h at a high current density of 5 mA cm^{-2} and a high areal capacity of 5 mAh cm^{-2}, 4 times longer than that of pristine Zn (20 h, Fig. S17 online). Under the depth of charge (DOC) of Zn of 51%, the

(002)-Zn electrode showed stable Zn plating/stripping cycling for more than 50 cycles at 10 mA cm^{-2} and 3 mAh cm^{-2}, which far outperformed the pristine Zn electrode with a short cycle-life of less than 10 cycles under the same test condition (Fig. S18 online). The electrodes after electrochemical cycling were characterized by SEM. The pristine Zn electrode after 40 cycles at 5 mA cm^{-2} and 2 mAh cm^{-2} showed a non-uniform surface with significant plate-like ZHS corrosion products (Fig. 5c and S16 online). Accordingly, due to the fast accumulation of resistive ZHS layers, the overpotential of the pristine Zn electrode increased after 40 cycles. In contrast, the (002)-Zn electrode after the same test condition exhibited a uniform surface under SEM and no corrosion products were detected by XRD (Fig. 5d and S16 online). Also, the overpotential of the (002)-Zn electrode remained stable after 40 cycles. These results suggest the important role of surface ZHS layer in suppressing corrosion side-reactions and improving the cycling stability of the (002)-Zn electrode. The high electrochemical reversibility and practicability of the as-achieved (002)-Zn electrode was also examined using full cells with MnO_2 cathodes. The cycling performance of pristine MnO_2||pristine Zn and MnO_2||(002)-Zn cells were shown in Fig. 5e-g. The MnO_2||(002)-Zn cell displayed a moderately high capacity of 83.6 mAh g^{-1} at 10 *C* for the initial cycle and its capacity retention was 92.7 % for 1000 cycles. As a sharp contrast, the MnO_2||pristine Zn cell only showed 34.9 % capacity retention after 100 cycles under the same test condition. Moreover, the pristine Zn electrode in MnO_2||pristine Zn cell showed a porous surface with a lot of pits after 100 cycles, while the (002)-Zn electrode in MnO_2||Zn cell exhibited a flat and uniform surface after 1000 cycles (Fig. S19 online), suggesting the good stability of (002)-Zn electrode due to the protection from the *in-situ* formed (001) ZHS. Besides, the MnO_2||(002)-Zn cell showed improved self-discharge rate and increased Coulombic efficiency in comparison to the MnO_2||pristine Zn cell (96 % for the MnO_2||(002)-Zn cell *vs*. 87 % for the MnO_2||pristine cell after resting for 12 h, Fig. S20 online). The MnO_2||(002)-Zn cell exhibited average discharge capacities of 288.6, 174.4, 134.9, 99.5, and 83.6 mAh g^{-1} at 0.1, 0.5, 1, 5, and 10 *C*, respectively, which far outperformed the MnO_2||pristine Zn cell that displayed average discharge capacities of 218.8, 134.1, 104.1, 68.6, and 62.3 mAh g^{-1} at 0.1, 0.5, 1, 5, and 10 *C* (Fig. S21 online). This result suggests the important role of ZHS layer in facilitating Zn^{2+}-ion diffusion at the anode/electrolyte interface. The above-demonstrated electrochemical results highlight the important role of crystal plane and surface regulation of metallic Zn in improving the electrochemical reversibility and stability, and show great promise of the (002)-Zn electrode for practical applications.

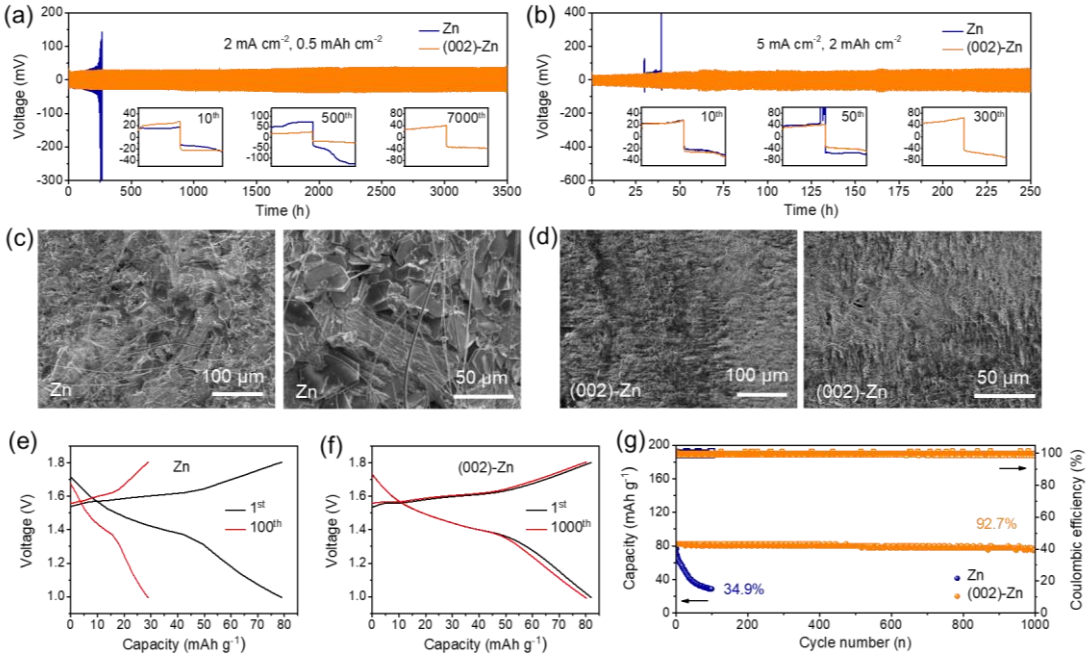

Fig. 5 Electrochemical performance of (002)-Zn electrode. Voltage profiles of Zn||Zn and (002)-Zn||(002)-Zn symmetric cells at (a) 2 mA cm^{-2} and 0.5 mAh cm^{-2}, and (b) 5 mA cm^{-2} and 2 mAh cm^{-2}. The insets in (a) and (b) show the expanded view at specific cycles. SEM images of (c) the pristine Zn electrode and (d) the (002)-Zn electrode after 40 cycles at 5 mA cm^{-2} and 2 mAh cm^{-2}. Some glass fibers from the separator are adhered on the cycled pristine Zn electrode and cannot be completely removed, suggesting the rough electrode surface. Discharge-charge voltage profiles of (e) MnO_2||Zn and (f) MnO_2||(002)-Zn cells. (g) Cycling stability of pristine MnO_2||Zn and MnO_2||(002)-Zn cells, suggesting the high electrochemical reversibility of the (002)-Zn electrode

4 Conclusions

In this work, we reported the spontaneous growth of horizontal ZHS layer with dominating (001) facet on the surface of Zn metal electrode with (002) texture in aqueous electrolyte, which possessed high ionic conductivity and low electrical conductivity and could work as an effective SEI to enable stable electrochemical cycling in aqueous electrolyte. The *in-situ* generated ZHS isolated the active Zn metal from aqueous electrolyte, and prevented corrosion side-reactions. At the same time, the low self-diffusion barrier of (002)-Zn electrode induced the horizontal deposition of metallic Zn and prevented its dendritic growth. As a result, the (002)-Zn electrode exhibited stable cycling for 3500 h with a low overpotential of 25 mV at 2 mA cm^{-2} and 0.5 mAh cm^{-2}. A MnO_2||(002)-Zn full cell also showed remarkable cycling stability under 10 *C* for 1000 cycles with 92.7% capacity retention. The SEI chemistry of (002)-Zn electrode demonstrated in this study would benefit the rational design of stabilized Zn electrode for advanced aqueous batteries and promote the large-scale application of aqueous Zn batteries.

Acknowledgments

Y. S. acknowledges the financial support by the Innovation Fund of Wuhan National Laboratory for Optoelectronics of Huazhong University of Science and Technology. Z. C. thanks the China Postdoctoral Science Foundation (No. 2018M640694, 2020T130223). Z. W. S. acknowledges the support of the Singapore National Research

Foundation (NRF-NRFF2017-04) and Agency for Science, Technology and Research (Central Research Fund Award). The authors would like to thank the Analytical and Testing Center of Huazhong University of Science and Technology as well as the Center for Nanoscale Characterization & Devices of Wuhan National Laboratory for Optoelectronics for providing the facilities to conduct the characterization. Special thanks to Miss. Xianhui Gao for her assistance with the EBSD.

Conflict of interest

All authors declare that they have no conflict of interest.

Author Contributions

Jindi Wang, Bao Zhang, Zhao Cai, and Yongming Sun conceived the project. Jindi Wang, Zhao Cai, and Renming Zhan performed the experiments. Wenyu Wang drew the schematic illustration. Bao Zhang and Jianjun Jiang performed the computational work. Jindi Wang, Bao Zhang, Zhao Cai, Li Wang, Zhi Wei Seh, Hong Li, and Yongming Sun wrote the manuscript. Yongming Sun supervised the project. All authors discussed the results and commented on the manuscript.

References

[1] Qi S, Wang H, He J, et al. Electrolytes enriched by potassium perfluorinated sulfonates for lithium metal batteries. Sci Bull, 2021, 66: 685-693.
[2] Dou Q, Wang Y, Wang A, et al. "Water in salt/ionic liquid" electrolyte for 2.8 V aqueous lithium-ion capacitor. Sci Bull, 2020, 65: 1812-1822.
[3] Chu S, Cui Y, Liu N. The path towards sustainable energy. Nat Mater, 2016, 16: 16-22.
[4] Service RF. Zinc aims to beat lithium batteries at storing energy. Science, 2021, 372: 890-891.
[5] Chen J, Yang Z, Liu G, et al. Reinforcing concentrated phosphate electrolytes with in-situ polymerized skeletons for robust quasi-solid lithium metal batteries. Energy Storage Mater, 2020, 25: 305-312.
[6] Huang J, Zhou J, Liang S. Guest pre-intercalation strategy to boost the electrochemical performance of aqueous zinc-ion battery cathodes. Acta Phys -Chim Sin, 2021, 37: 2005020.
[7] Qiu H, Du X, Zhao J, et al. Zinc anode-compatible in-situ solid electrolyte interphase via cation solvation modulation. Nat Commun, 2019, 10: 5374.
[8] Zheng J, Zhao Q, Tang T, et al. Reversible epitaxial electrodeposition of metals in battery anodes. Science, 2019, 366: 645-648.
[9] Chu Y, Zhang S, Wu S, et al. In situ built interphase with high interface energy and fast kinetics for high performance Zn metal anodes. Energy Environ Sci, 2021, 14: 3609-3620.
[10] Chao D, Zhou W, Ye C, et al. An electrolytic Zn-MnO_2 battery demonstrated for high-voltage and scalable energy storage. Angew Chem Int Ed, 2019, 58: 7823-7828.
[11] Parker JF, Chervin CN, Pala IR, et al. Rechargeable nickel-3D zinc batteries: An energy-dense, safer alternative to lithium-ion. Science, 2017, 356: 415-418.
[12] Zheng J, Bock DC, Tang T, et al. Regulating electrodeposition morphology in high-capacity aluminium and zinc battery anodes using interfacial metal–substrate bonding. Nat Energy, 2021, 6: 398-406.
[13] Zhou M, Guo S, Li J, et al. Surface-preferred crystal plane for a stable and reversible zinc anode. Adv Mater, 2021, 33: 2100187.
[14] Wang J, Cai Z, Xiao R, et al. A chemically polished zinc metal electrode with a ridge-like structure for cycle-stable aqueous batteries. ACS Appl Mater Interfaces, 2020, 12: 23028-23034.
[15] Pan H, Shao Y, Yan P, et al. Reversible aqueous zinc/manganese oxide energy storage from conversion reactions. Nat Energy, 2016, 1: 16039.
[16] Hao J, Yuan L, Ye C, et al. Boosting zinc electrode reversibility in aqueous electrolytes by using low-cost antisolvents. Angew Chem Int Ed, 2021, 60: 7366-7375.
[17] Yang Q, Li Q, Liu Z, et al. Dendrites in Zn-based batteries. Adv Mater, 2020, 32: 2001854.
[18] Ma L, Li Q, Ying Y, et al. Toward practical high-areal-capacity aqueous zinc-metal batteries: Quantifying hydrogen evolution and a solid-ion conductor for stable zinc anodes. Adv Mater, 2021, 33: 2007406.

[19] Cai Z, Ou Y, Wang J, et al. Chemically resistant Cu–Zn/Zn composite anode for long cycling aqueous batteries. Energy Storage Mater, 2020, 27: 205-211.
[20] Sui Y, Ji X. Anticatalytic strategies to suppress water electrolysis in aqueous batteries. Chem Rev, 2021, 121: 6654-6695.
[21] Zhu M, Hu J, Lu Q, et al. A patternable and in situ formed polymeric zinc blanket for a reversible zinc anode in a skin-mountable microbattery. Adv Mater, 2021, 33: 2007497.
[22] Zhu M, Wang X, Tang H, et al. Antifreezing hydrogel with high zinc reversibility for flexible and durable aqueous batteries by cooperative hydrated cations. Adv Funct Mater, 2020, 30: 1907218.
[23] Cai Z, Ou Y, Zhang B, et al. A replacement reaction enabled interdigitated metal/solid electrolyte architecture for battery cycling at 20 mA cm^{-2} and 20 mAh cm^{-2}. J Am Chem Soc, 2021, 143: 3143-3152.
[24] Xie X, Liang S, Gao J, et al. Manipulating the ion-transfer kinetics and interface stability for high-performance zinc metal anodes. Energy Environ Sci, 2020, 13: 503-510.
[25] Liu X, Yang F, Xu W, et al. Zeolitic imidazolate frameworks as Zn^{2+} modulation layers to enable dendrite-free Zn anodes. Adv Sci, 2020, 7: 2002173.
[26] Yang Y, Liu C, Lv Z, et al. Redistributing Zn-ion flux by interlayer ion channels in Mg-Al layered double hydroxide-based artificial solid electrolyte interface for ultra-stable and dendrite-free Zn metal anodes. Energy Storage Mater, 2021, 41: 230-239.
[27] Chen L, Wang K, Xie X, et al. Effect of vinylene carbonate (VC) as electrolyte additive on electrochemical performance of Si film anode for lithium ion batteries. J Power Sources, 2007, 174: 538-543.
[28] Yan C, Li H-R, Chen X, et al. Regulating the inner helmholtz plane for stable solid electrolyte interphase on lithium metal anodes. J Am Chem Soc, 2019, 141: 9422-9429.
[29] Zhan R, Zhang Y, Chen H, et al. High-rate and long-life sodium-ion batteries based on sponge-like three-dimensional porous Na-rich ferric pyrophosphate cathode material. ACS Appl Mater Interfaces, 2019, 11: 5107-5113.
[30] Wang T, Li C, Xie X, et al. Anode materials for aqueous zinc ion batteries: Mechanisms, properties, and perspectives. ACS Nano, 2020, 14: 16321-16347.
[31] Yi Z, Chen G, Hou F, et al. Strategies for the stabilization of Zn metal anodes for Zn‐ion batteries. Adv Energy Mater, 2020, 11: 2003065.
[32] Hao J, Li B, Li X, et al. An in-depth study of Zn metal surface chemistry for advanced aqueous Zn-ion batteries. Adv Mater, 2020, 32: 2003021.
[33] Cao L, Li D, Pollard T, et al. Fluorinated interphase enables reversible aqueous zinc battery chemistries. Nat Nanotechnol, 2021, 16: 902-910.
[34] Zeng X, Mao J, Hao J, et al. Electrolyte design for in situ construction of highly Zn^{2+} -conductive solid electrolyte interphase to enable high-performance aqueous Zn-ion batteries under practical conditions. Adv Mater, 2021, 33: 2007416.
[35] Li D, Cao L, Deng T, et al. Design of a solid electrolyte interphase for aqueous Zn batteries. Angew Chem Int Ed, 2021, 60: 13035-13041.
[36] Hohenberg P, Kohn W. Inhomogeneous electron gas. Phys Rev, 1964, 136: B864-B871.
[37] Kohn W, Sham LJ. Self-consistent equations including exchange and correlation effects. Phys Rev, 1965, 140: A1133-A1138.
[38] Kresse G, Hafner J. Ab initio molecular dynamics for liquid metals. Phys Rev B, 1993, 47: 558-561.
[39] Blöchl PE. Projector augmented-wave method. Phys Rev B, 1994, 50: 17953-17979.
[40] Kresse G, Furthmüller J. Efficient iterative schemes for ab initio total-energy calculations using a plane-wave basis set. Phys Rev B, 1996, 54: 11169-11186.
[41] Perdew JP, Burke K, Ernzerhof M. Generalized gradient approximation made simple. Phys Rev Lett, 1996, 77: 3865-3868.
[42] Grimme S, Antony J, Ehrlich S, et al. A consistent and accurate ab initio parametrization of density functional dispersion correction (DFT-D) for the 94 elements H-Pu. J Chem Phys, 2010, 132: 154104.
[43] Monkhorst HJ, Pack JD. Special points for brillouin-zone integrations. Phys Rev B, 1976, 13: 5188-5192.
[44] Fan X, Ji X, Han F, et al. Fluorinated solid electrolyte interphase enables highly reversible solid-state Li metal battery. Sci Adv, 2018, 4: 10.
[45] Momma K, Izumi F. VESTA 3for three-dimensional visualization of crystal, volumetric and morphology data. J Appl Crystallogr, 2011, 44: 1272-1276.
[46] Plimpton S. Fast parallel algorithms for short-range molecular dynamics. J Comput Phys, 1995, 117: 1-19.

[47] Jang H-S, Seol D, Lee B-J. Modified embedded-atom method interatomic potentials for Mg–Al–Ca and Mg–Al–Zn ternary systems. J Magnes Alloys, 2021, 9: 317-335.
[48] Zhou X, Lu Y, Zhang Q, et al. Exploring the interfacial chemistry between zinc anodes and aqueous electrolytes via an in situ visualized characterization system. ACS Appl Mater Interfaces, 2020, 12: 55476-55482.
[49] Verma V, Kumar S, Manalastas W, et al. Undesired reactions in aqueous rechargeable zinc ion batteries. ACS Energy Lett, 2021, 6: 1773-1785.
[50] Jin S, Huang M, Kwon Y, et al. Colossal grain growth yields single-crystal metal foils by contact-free annealing. Science, 2018, 362: 1021-1025.
[51] Kim Y-J, Kwon SH, Noh H, et al. Facet selectivity of Cu current collector for Li electrodeposition. Energy Storage Mater, 2019, 19: 154-162.
[52] Zhao Z, Zhao J, Hu Z, et al. Long-life and deeply rechargeable aqueous Zn anodes enabled by a multifunctional brightener-inspired interphase. Energy Environ Sci, 2019, 12: 1938-1949.

Jindi Wang received his B.S. degree from Beijing University of Chemical Technology in 2018. He is currently a Ph.D. student in Wuhan National Laboratory for Optoelectronics at Huazhong University of Science and technology. His research interest focuses on the aqueous Zn metal batteries.

Bao Zhang is a Postdoc of school of optical and electronic information, Huazhong University of Science and Technology. His research focus is electrolyte electrochemistry and solid electrolyte interphase design for energy storage.

Zhao Cai received his B.S. and Ph.D. degree from Beijing University of Chemical Technology in 2012 and 2018, respectively. He was a visiting assistant in research at Yale University in 2016-2017 and is now a Postdoc at Wuhan National Laboratory for Optoelectronics, Huazhong University of Science and Technology. His research focuses on developing novel transition metal electrode materials for key energy conversion and storage processes, such as electrocatalysis and aqueous batteries.

Yongming Sun received his Ph.D. degree from Huazhong University of Science and Technology in 2012. He is currently a professor at Wuhan National Laboratory for Optoelectronics at Huazhong University of Science and Technology. His research focuses on materials for rechargeable Li-based batteries, Na-based batteries and Zn-based batteries.

Graphical abstract

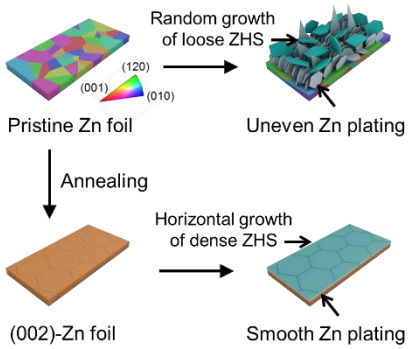

Conformal growth of homogeneous and dense (001) plane-dominated zinc hydroxide sulfate layer was realized on (002)-textured Zn metal foil electrode, which achieved stable interface chemistry by hindering further corrosion reaction and promoting horizontal electrochemical plating of metallic Zn, thus improving the electrochemical reversibility of (002)-textured Zn electrode and aqueous Zn batteries.